

Fully developed laminar mixed convection in uniformly heated horizontal annular ducts

L.P.M. Colombo, A. Lucchini*, A. Muzzio

Dipartimento di Energia, Politecnico di Milano, Via Lambruschini, 4, 20156 Milano, MI, Italy

Received 3 January 2014

Received in revised form 7 November 2014

Accepted 9 March 2015

1. Introduction

Laminar internal flows are often encountered in industrial situations, such as compact heat exchangers, exchangers designed for application in chemical and food processes, cooling of electronic equipment, etc., in which small dimensions and/or low velocities are employed. These flows with heat transfer may be strongly influenced by buoyancy forces arising from temperature differences in the fluid under the influence of the gravitational force field. In fact, experimental and theoretical work evidences that both the effects of natural convection and forced convection may be of comparable order in many cases of practical interest. In this circumstance, the flow orientation with respect to gravity becomes an important parameter. The laminar mixed convection of a fluid in horizontal ducts has been the subject of a number of studies both experimental and numerical, which cover a range of geometrical configurations and boundary conditions. Among the various geometries, the fluid flow and heat transfer between two horizontal concentric cylinders has attracted considerable attention because of its technical importance, as it is present in numerous engineering applications such as gas-cooled electrical cables, and double-pipe

heat exchangers, just to mention a few examples. From the analysis of the available literature, it appears that most of the studies are relevant to Newtonian fluids, constant thermo-physical properties, stationary bounding surfaces, and uniform thermal boundary conditions along the girth of the cylinders [1–11]. Only a limited number of authors have considered different conditions such as constant heat flux along the periphery of the inner cylinder [12], forced convection due to a cooled rotating outer cylinder [13], temperature-dependent viscosity [14], thermodependent non-Newtonian fluids [15], and non-uniform circumferential heating [16]. Finally, Chenier et al. [17] performed numerically a linear stability analysis of a fully developed mixed convection flow of air in an annular horizontal duct.

The present study deals with a numerical solution of fully developed laminar flow and heat transfer in horizontal concentric annuli, based on a Galerkin spectral method. The fully developed situation is an asymptotic condition that prevails for large values of the axial coordinates. For purely forced convection in concentric annular ducts both hydrodynamic entrance length and thermal entrance length, the latter for the four fundamental thermal boundary conditions, have been studied by several authors; the obtained results have been compiled by Shah and London and presented in Ref. [18] in tabular form. In the case of combined forced and free convection, only few studies are available on entrance region effect [7–12]. None of them systematically treats

* Corresponding author.

E-mail address: andrea.lucchini@polimi.it (A. Lucchini).

the determination of hydrodynamic and thermal entrance lengths; only some indication can be found in the case of inner wall heated. Ciampi et al. [7] used water as a working fluid flowing in annuli with $\eta = 0.46$ and 0.63 . These authors claim that in general a length of 4–6 hydraulic diameters is needed to obtain a linear temperature distribution that is to reach the fully developed region. Islam et al. [10,12], noticed from their experimental runs that with water at $2.14 < Pr < 5.34$ and $1/\eta = 1.75, 2.14$ the entrance lengths are very small and less than 3.5 times the hydraulic diameter. From the analysis of their numerical results, they conclude that higher Pr leads to early development of the flow. Furthermore, the thermal entrance length is relatively smaller for smaller η . However, according to them, it is difficult to identify an entrance length in these cases because the Nusselt number goes through a minimum, then a maximum and finally approaches a constant value. Therefore, while the assumption of fully developed fields is, in general, rather restrictive, only for very short ducts the use of the results presented here is inappropriate.

Among the possible combinations of thermal boundary conditions, the selected ones consist in axially uniform heat flow per unit length, uniform temperature along the periphery of the heated wall, thermal insulation on the remaining surface. Either heating at the inner wall or heating at the outer wall have been considered. The choice of these case studies is motivated both by the lack of complete investigations and by the evidence of significant discrepancies between the results of numerical simulations and experimental data in the available literature. In particular, the numerical study of Nিকে and Patankar [5] and the experimental investigation of Ciampi et al. [7] consider only the case of heating at the inner wall. On the other hand, at the best knowledge of the authors, only the paper of Hattori [1], reporting both experimental data, numerical simulations and the perturbation analysis takes into account the case of outer wall heated. Since for heating at the inner wall very good agreement with the findings of Nিকে and Patankar has been found, the case of outer wall heated has been studied more deeply, considering a larger number of diameter ratios. Correlations between the relevant dimensionless parameters have been developed as well and compared with the available data and correlations.

2. Problem formulation and governing equations

We consider the steady laminar flow of a Newtonian fluid in a long horizontal annular duct subject to axially uniform heat flow per unit length. Among the various possible thermal boundary conditions, reference is made to uniform temperature along the girth of the inner tube and to adiabatic outer surface and to uniform temperature along the girth of the outer tube and to adiabatic inner surface. According to [18] for this fundamental boundary condition, the wall thermal conductivity is implicitly assumed to be zero in the axial direction and infinite in the peripheral direction. If the local heat transfer coefficient varies along the girth of the heated pipe, as it is the case of this study or for noncircular ducts, it may be difficult to achieve in practice the stated boundary condition. However, it may be considered a limiting case of more realistic boundary conditions and together with the other limiting case of constant heat flux, it is the most frequently investigated fundamental boundary condition in the literature. Referring to the usual Oberbeck–Boussinesq approximation, the thermophysical properties of the fluid are constant except density, which is supposed to be dependent only on temperature according to a linear relationship, in the buoyancy term. Furthermore, the effects of viscous dissipation in the energy equation are neglected.

If we disregard the density variation along the axis, sufficiently far from the duct inlet the problem admits a similarity solution [19]

with velocity, pressure and temperature differences in the cross section independent from the axial coordinate. This assumption has been thoroughly discussed by Nিকে and Patankar [5] and it is shown that disregarding the density variation along the axis is justified for values of the ratio between the Richardson number and the Prandtl number less than unity. This condition is easily verified for large Prandtl numbers. On the other hand, for moderate Prandtl numbers, the assumption is justified for small values of the Richardson number. As a consequence, in any case, the Richardson number disappears in the formulation of the problem. In the fully developed region, temperature, T , and pressure, p , through the duct vary linearly with the distance along the axis. That is, in the cylindrical coordinates (r, ψ, z) ,

$$T(r, \psi, z) = \tau z + T'(r, \psi) \quad (1)$$

$$p(r, \psi, z) = \gamma z + p'(r, \psi) \quad (2)$$

where τ and γ are the axial temperature and pressure gradients, respectively.

Under the stated assumptions and with reference to Fig. 1, the governing equations are then

$$\frac{1}{r} \frac{\partial}{\partial r} (ru) + \frac{1}{r} \frac{\partial v}{\partial \psi} = 0 \quad (3)$$

$$\rho \left(u \frac{\partial u}{\partial r} + \frac{v}{r} \frac{\partial u}{\partial \psi} - \frac{v^2}{r} \right) = -\frac{\partial p}{\partial r} + \mu \left[\frac{\partial}{\partial r} \left(\frac{1}{r} \frac{\partial}{\partial r} (ru) \right) + \frac{1}{r^2} \frac{\partial^2 u}{\partial \psi^2} - \frac{2}{r^2} \frac{\partial v}{\partial \psi} \right] + \rho \beta g (T_w - T) \cos \psi \quad (4)$$

$$\rho \left(u \frac{\partial v}{\partial r} + \frac{v}{r} \frac{\partial v}{\partial \psi} + \frac{uv}{r} \right) = -\frac{1}{r} \frac{\partial p}{\partial \psi} + \mu \left[\frac{\partial}{\partial r} \left(\frac{1}{r} \frac{\partial}{\partial r} (rv) \right) + \frac{1}{r^2} \frac{\partial^2 v}{\partial \psi^2} + \frac{2}{r^2} \frac{\partial u}{\partial \psi} \right] - \rho \beta g (T_w - T) \sin \psi \quad (5)$$

$$\rho \left(u \frac{\partial w}{\partial r} + \frac{v}{r} \frac{\partial w}{\partial \psi} \right) = -\frac{\partial p}{\partial z} + \mu \left[\frac{1}{r} \frac{\partial}{\partial r} \left(r \frac{\partial w}{\partial r} \right) + \frac{1}{r^2} \frac{\partial^2 w}{\partial \psi^2} \right] \quad (6)$$

$$\rho c \left(u \frac{\partial T}{\partial r} + \frac{v}{r} \frac{\partial T}{\partial \psi} + w \frac{\partial T}{\partial z} \right) = k \left[\frac{1}{r} \frac{\partial}{\partial r} \left(r \frac{\partial T}{\partial r} \right) + \frac{1}{r^2} \frac{\partial^2 T}{\partial \psi^2} \right] \quad (7)$$

where u, v, w denote the velocity components, ρ is the density in the reference state, μ is the viscosity, β the coefficient of thermal

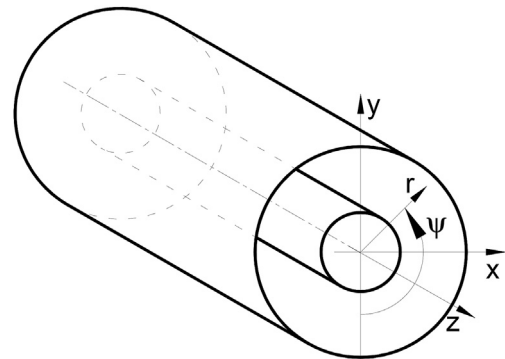


Fig. 1. Geometry and coordinate system.

expansion, c the specific heat, k the thermal conductivity, g the acceleration due to gravity, and $T_w(z)$ the local temperature of the inner pipe wall. In the momentum Eqs. (4) and (5) we expressed the buoyancy force relative to fluid at the same level adjacent to the inner duct wall and we embodied the remaining distribution of force into the pressure, p . Furthermore, from Eqs. (1) and (2) it follows that

$$\frac{\partial T}{\partial z} = \tau = \text{const.} \quad \text{and} \quad \frac{\partial p}{\partial z} = \gamma = \text{const.} \quad (8)$$

Let r_i be the outer radius of the inner pipe, r_e the inner radius of the outer pipe and $\eta = r_i/r_e$.

The Eqs. (3)–(7) can be reduced to non dimensional form by the transformations:

$$R = \frac{r}{r_e}, \quad U = \frac{uD_H}{\alpha}, \quad V = \frac{vD_H}{\alpha}, \quad W = \frac{w}{\bar{w}^*}, \quad P = \frac{p}{p^*}, \quad \vartheta = \frac{T_w - T}{\Delta T^*} \quad (9)$$

where $D_H = 2(r_e - r_i)$ is the hydraulic diameter and α is the thermal diffusivity.

In non-dimensionalizing the axial velocity, w , we used a scale \bar{w}^* referred to γ , namely the average velocity for laminar flow through an unheated annular duct, that is [20].

$$\bar{w}^* = -\frac{\gamma r_e^2}{8\mu} \left[\frac{1 - \eta^4}{1 - \eta^2} - \frac{1 - \eta^2}{\ln\left(\frac{1}{\eta}\right)} \right] \quad (10)$$

while the scale for the temperature was chosen as $\Delta T^* = PrReD_H\tau = PeD_H\tau$ where $Pr = c\mu/k$ is the Prandtl number, $Re = \frac{\rho\bar{w}D_H}{\mu}$ is the Reynolds number and $Pe = PrRe$ is the Péclet

number. In order to identically satisfy the continuity Eq. (3) and eliminating the pressure by cross differentiation and subtraction of the momentum Eqs. (4) and (5), the following system of three partial differential equations results:

$$\Delta^2 f - \frac{\varepsilon}{Pr} \frac{1}{R} J(f, \Delta f) = -\varepsilon^2 Pe Ra \frac{1}{R} J(\vartheta, R \cos \psi) \quad (12)$$

$$\Delta W + \delta = \frac{\varepsilon}{Pr} \frac{1}{R} J(f, W) \quad (13)$$

$$\Delta \vartheta + \varepsilon^2 W = \varepsilon \frac{1}{R} J(f, \vartheta) \quad (14)$$

where $\varepsilon = 1/2(1 - \eta)$, $\delta = \frac{8}{\frac{1-\eta^4}{1-\eta^2} - \frac{1-\eta^2}{\ln(\frac{1}{\eta})}}$, $Ra = \frac{g\tau\rho^2 c D_H^4}{\mu k}$ is the Rayleigh number.

In the above equations Δ^2 and Δ denote the biharmonic and the Laplace operators in the (R, ψ) coordinates, respectively, and

$$J(A, B) = \frac{\partial A}{\partial R} \frac{\partial B}{\partial \psi} - \frac{\partial A}{\partial \psi} \frac{\partial B}{\partial R} \quad (15)$$

denotes the Jacobian operator.

Since the problem is symmetric about the vertical plane passing through the axis of the duct, only one-half of the annular cross section may be considered. The relevant boundary conditions are then

$$\begin{aligned} R = \eta, \quad 0 \leq \psi \leq \pi, \quad f = \frac{\partial f}{\partial R} = W = 0, \quad & \begin{cases} \vartheta = 0 & \text{adiabatic outer tube} \\ \frac{\partial \vartheta}{\partial R} = 0 & \text{adiabatic inner tube} \end{cases} \\ R = 1, \quad 0 \leq \psi \leq \pi, \quad f = \frac{\partial f}{\partial R} = W = 0, \quad & \begin{cases} \vartheta = 0 & \text{adiabatic inner tube} \\ \frac{\partial \vartheta}{\partial R} = 0 & \text{adiabatic outer tube} \end{cases} \\ \psi = \begin{cases} 0 \\ \pi \end{cases} \quad \eta \leq R \leq 1, \quad f = \frac{\partial^2 f}{\partial \psi^2} = \frac{\partial W}{\partial \psi} = \frac{\partial \vartheta}{\partial \psi} = 0 \end{aligned} \quad (16)$$

number. From the energy balance, it can be shown that an equivalent expression for the reference temperature difference is $\Delta T^* = 4 \frac{\dot{Q}}{k} \frac{\eta}{1+\eta} \frac{\bar{w}^*}{w}$ for the case of inner wall heating, and $\Delta T^* = 4 \frac{\dot{Q}}{k} \frac{1}{1+\eta} \frac{\bar{w}^*}{w}$ for the case of outer wall heating. Apart from the trivial case $k = 0$, the reference temperature difference is well defined even for $Pr \rightarrow \infty$. As a consequence of the former choices, the pressure scale turns out to be $p^* = 2 \frac{\mu^2}{\rho D_H^2} (1 - \eta)$.

Introducing the non dimensional stream function f , defined by

$$U = -\frac{1}{R} \frac{\partial f}{\partial \psi}, \quad V = \frac{\partial f}{\partial R} \quad (11)$$

3. Method of solution

In order to obtain a solution of the problem (8)–(11) we use a Galerkin spectral method [21,22]. An approximate solution for each of the unknown fields f , W , ϑ is sought as a truncated expansion in terms of trial functions satisfying the boundary conditions (11). We set

$$f^{N,M}(R, \psi) = \sum_{i=1}^N \sum_{j=1}^M C_{ij} f_{ij} \Psi_{ij}(R, \psi) = \sum_{i=1}^N \sum_{j=1}^M C_{ij} f_{ij} \Phi_j(R) \sin(i\psi) \quad (17)$$

where f_{ij} are the expansion coefficients and the trial functions Φ have the form

$$\begin{aligned}\Phi_j(R) &= \int_{\eta}^R dt \int_{\eta}^t P_{j+1} \left(\frac{2}{1-\eta} \xi - \frac{1+\eta}{1-\eta} \right) d\xi \\ &= \int_{\eta}^R (R-t) P_{j+1} \left(\frac{2}{1-\eta} t - \frac{1+\eta}{1-\eta} \right) dt\end{aligned}\quad (18)$$

and P_{j+1} denote Legendre polynomials.

By known properties of the Legendre polynomials [21] the following expression for the Φ_j results

$$\begin{aligned}\Phi_j(R) &= \left(\frac{1-\eta}{2} \right)^2 \frac{1}{2j+3} \left(\frac{1}{2j+5} P_{j+3}(\xi) - \frac{2(2j+3)}{(2j+5)(2j+1)} P_{j+1}(\xi) \right. \\ &\quad \left. + \frac{1}{2j+1} P_{j-1}(\xi) \right)\end{aligned}\quad (19)$$

where $\xi = \frac{2}{1-\eta} R - \frac{1+\eta}{1-\eta}$.

By applying the same approach to the axial velocity and temperature fields, we assume the approximate representations for W and ϑ

$$\begin{aligned}W^{N,M} &= W_0(R) + \overline{W}^{N,M}(R, \psi) = W_0(R) + \sum_{i=0}^N \sum_{j=1}^M Cw_{ij} w_{ij} \Omega_{ij}(R, \psi) \\ \vartheta^{N,M} &= \vartheta_0(R) + \overline{\vartheta}^{N,M}(R, \psi) = \vartheta_0(R) + \sum_{i=0}^N \sum_{j=1}^M Ct_{ij} \vartheta_{ij} \Theta_{ij}(R, \psi)\end{aligned}\quad (20)$$

$W_0(R)$ and $\vartheta_0(R)$ are axial velocity and temperature distributions in the absence of natural convection. $W_0(R)$ is expressed by the following relationship

$$W_0(R) = \frac{2}{\frac{1-\eta^4}{1-\eta^2} - \frac{1-\eta^2}{\ln(\frac{1}{\eta})}} \left(1 - R^2 - \frac{1-\eta^2}{\ln(\frac{1}{\eta})} \ln\left(\frac{1}{R}\right) \right)\quad (21)$$

$\vartheta_0(R)$ has different representations according to whether the active heat transfer surface is the inner or the outer tube. In the first case we have

$$\begin{aligned}\vartheta_0(R) &= \frac{1}{2 \left(\frac{1-\eta^4}{1-\eta^2} - \frac{1-\eta^2}{\ln(\frac{1}{\eta})} \right) (1-\eta)^2} \\ &\quad \cdot \left(\left(R^2 - \eta^2 - \ln\left(\frac{R}{\eta}\right) \right) \frac{1 + \frac{(1-\eta^2)}{\ln(\eta)}}{4} \right. \\ &\quad \left. - \frac{(R^4 - \eta^4)}{16} - \frac{(1-\eta^2)}{4 \ln(\eta)} \left(R^2 \ln(R) - \eta^2 \ln(\eta) \right) \right)\end{aligned}\quad (22)$$

while, in the second one, the proper expression is

$$\begin{aligned}\vartheta_0(R) &= \frac{1}{2 \left(\frac{1-\eta^4}{1-\eta^2} - \frac{1-\eta^2}{\ln(\frac{1}{\eta})} \right) (1-\eta)^2} \\ &\quad \cdot \left(\frac{R^2}{4} - \frac{R^4}{16} - \frac{3}{16} + \frac{(1-\eta^2)}{\ln(\frac{1}{\eta})} \left(\frac{R^2 \ln(R)}{4} - \frac{R^2}{4} + \frac{1}{4} \right. \right. \\ &\quad \left. \left. - \eta \left(\frac{\eta \ln(\eta)}{2} - \frac{\eta}{4} \right) \ln(R) \right) - \eta \left(\frac{\eta}{2} - \frac{\eta^3}{4} \right) \ln(R) \right)\end{aligned}\quad (23)$$

w_{ij} and ϑ_{ij} are the unknown coefficients of the truncated expansions and the trial functions are

$$\begin{aligned}\Omega_{ij}(R, \psi) &= \int_{\eta}^R P_j \left(\frac{2}{1-\eta} t - \frac{1+\eta}{1-\eta} \right) dt \\ \cos(i\psi) &= \frac{1-\eta}{2} \frac{1}{2j+1} (P_{j+1}(\xi) - P_{j-1}(\xi)) \cos(i\psi)\end{aligned}\quad (24)$$

and, when the active surface of heat transfer is the inner tube,

$$\Theta_{ij}(R, \psi) = \left(P_{j-1}(\xi) + \frac{(2j+1)}{(j+1)^2} P_j(\xi) - \frac{j^2}{(j+1)^2} P_{j+1}(\xi) \right) \cos(i\psi)\quad (25)$$

while, in the case of heat transfer at the outer tube, it is sufficient to change ξ into $-\xi$ in the above expression.

We note that, while the coefficients of the truncated expansions are actually functions of N and M , we omitted signalling this dependence in the notation for the sake of simplicity.

Let Ω be the half annulus ($\eta \leq R \leq 1$, $0 \leq \psi \leq \pi$) and let (\cdot, \cdot) denote the $L^2(\Omega)$ inner product $(A, B) = \int_{\Omega} A \cdot B d\Omega$.

The approximate solutions will not satisfy Eqs. (12)–(14), i.e. after substitution of $f^{N,M}$, $W^{N,M}$ and $\vartheta^{N,M}$ into the differential equations the residuals will not vanish everywhere. The Galerkin method results by demanding that the residuals are orthogonal to the trial functions with respect to the $L^2(\Omega)$ metric. The coefficients Cf_{ij} , Cw_{ij} and Ct_{ij} are determined by assuming as normalising condition the energy norms of the biharmonic operator in the first case and of the Laplace operator in the other two cases, with the boundary conditions (16). Besides, by taking into account that $\Delta W_0 + \delta = 0$ and $\Delta \vartheta_0 + \varepsilon^2 W_0 = 0$ we obtain the following system of nonlinear algebraic equations

$$\begin{aligned}(\Delta f^{N,M}, \Delta \Psi_{ij}) + \frac{\varepsilon}{\text{Pr}} \left(\frac{1}{R} J(f^{N,M}, \Psi_{ij}), \Delta f^{N,M} \right) \\ = -\varepsilon^2 \text{PeRa} \left(\frac{1}{R} J(\vartheta^{N,M}, R \cos \psi), \Psi_{ij} \right)\end{aligned}\quad (26)$$

with $i = 1, 2, \dots, N$ and $j = 1, 2, \dots, M$,

$$\begin{aligned}(\nabla \overline{W}^{N,M}, \nabla \Omega_{ij}) + \frac{\varepsilon}{\text{Pr}} \left(\frac{1}{R} J(f^{N,M}, \overline{W}^{N,M}), \Omega_{ij} \right) \\ = -\frac{\varepsilon}{\text{Pr}} \left(\frac{1}{R} J(f^{N,M}, W_0), \Omega_{ij} \right)\end{aligned}\quad (27)$$

$$\begin{aligned}
& (\nabla \bar{\vartheta}^{N,M}, \nabla \Theta_{ij}) + \varepsilon \left(\frac{1}{R} J(f^{N,M}, \bar{\vartheta}^{N,M}), \Theta_{ij} \right) \\
& = -\varepsilon \left(\frac{1}{R} J(f^{N,M}, \vartheta_0), \Theta_{ij} \right) + \varepsilon^2 \left(\bar{W}^{N,M}, \Theta_{ij} \right)
\end{aligned} \quad (28)$$

with $i = 0, 1, \dots, N$ and $j = 1, 2, \dots, M$.

In working out the above equations use was made of the equalities

$$\begin{aligned}
& (\Delta^2 f^{N,M}, \psi_{ij}) = (\Delta f^{N,M}, \Delta \psi_{ij}) \\
& -(\Delta \bar{W}^{N,M}, \Omega_{ij}) = (\nabla \bar{W}^{N,M}, \nabla \Omega_{ij}) \\
& -(\Delta \bar{\vartheta}^{N,M}, \Theta_{ij}) = (\nabla \bar{\vartheta}^{N,M}, \nabla \Theta_{ij}) \\
& -\left(\frac{1}{R} J(f^{N,M}, \Delta f^{N,M}), \psi_{ij} \right) = \left(\frac{1}{R} J(f^{N,M}, \psi_{ij}), \Delta f^{N,M} \right)
\end{aligned} \quad (29)$$

that may be easily verified by integrating by parts and noticing that the integrated parts vanish because of the boundary conditions.

The Eq. (28) were supplemented with one more equation obtained by integrating Eq. (10) over Ω , that is by requiring the fulfilment of the overall energy balance.

The over-determined system (26)–(28) has been solved iteratively. Starting from an initial guess f° and ϑ° one solves (12) with respect to f . Since this subsystem is nonlinear, it was solved iteratively, after linearization according to the Newton–Raphson technique, until a convergence criterion is met. The selected criterion was $\frac{\|f^{n+1} - f^n\|}{\|f^{n+1}\|} \leq \zeta$ where the superscript refers to the number of iteration and ζ is an assigned tolerance which was taken to be $5 \cdot 10^{-8}$, typically. With the new f one solves (27) with respect to \bar{W} and, successively (28) in the least squares sense for $\bar{\vartheta}$, being these two subsystems linear in the stated unknowns. The whole procedure is repeated until achievement of convergence, tested on $\bar{\vartheta}$ according to the same criterion used in the inner iteration. The scheme proved to be convergent at the larger values of the $PeRa$ parameter, only by under-relaxing the unknowns of the temperature field

$$\vartheta^{*n+1} = \omega \vartheta^{n+1} + (1 - \omega) \vartheta^n \quad (30)$$

where the star indicates the relaxed variables. A value of ω decreasing with $PeRa$ and equal to 0.1 at the highest values of this parameter produced a monotonic convergence in all the tested cases and showed to accelerate convergence also when under-relaxation was not strictly necessary.

The inner products that constitute the elements of the various matrices were computed analytically as far as possible. While the integration with respect to the ψ -coordinate poses no problem to be performed analytically, it is not always so with respect to the R -coordinate. Therefore, when needed, numerical quadrature was carried out by the adaptive Simpson's rule.

4. Results and discussion

As it can be seen from the dimensionless formulation of the problem, the relevant parameters of this study are the product of the Péclet number and the Rayleigh number, $PeRa$, the Prandtl number, Pr , and the ratio between the outer radius of the inner pipe and the inner radius of the outer pipe, η .

Results have been obtained for $PeRa$ values up to 10^7 , for three values of Pr , namely 0.7, 5 and ∞ , for $\eta = 0.2$ in the case of the inner wall heated and for $\eta = 0.2, 0.4$ and 0.6 in the case of the outer wall heated.

In order to choose a suitable number of degree of freedom in the approximate solution, such as to achieve a good compromise between accuracy and computing time, numerical experiments were made by increasing M and N . From these calculations it was observed that, for increasing number of coordinate functions, the coefficients exhibited the tendency to stabilize quickly and, after a certain number depending on the values of the parameters, to decay rapidly. With $M = 15$ and $N = 20$ the results showed that in almost all the cases there were still modes practically inactivated. Therefore, this truncation was considered suitable in the whole of the examined cases with the exception, with reference to the outer wall heated, of $\eta = 0.6, Pr = 0.7$ and $PeRa > 7 \cdot 10^6$ in which the onset of spurious vortical structures required a greater number of angular modes, namely $N = 25$, for a proper description of flow and temperature fields.

To save computing time, all the numerical runs were started with input data derived from a previous calculation at a smaller value of the $PeRa$ or Pr numbers, at constant η .

In the following, we present results that include details of the flow and temperature fields in addition to local and average Nusselt numbers and the effect of natural convection on the flow-rate, distinguishing between inner wall heated and outer wall heated.

4.1. Inner wall heated

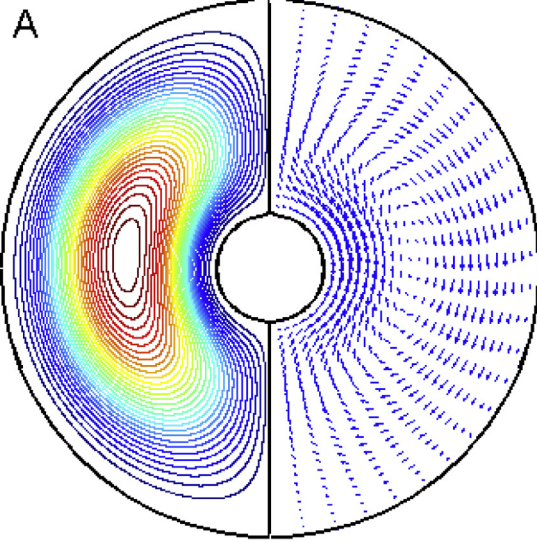
4.1.1. Streamline maps and velocity field

Representative streamline maps and structure of the secondary flow are displayed in Fig. 2 for different $PeRa$ values and $Pr = 0.7$. Owing to the symmetry about the vertical diameter only one half of the cross section need to be considered; the streamlines are then plotted in the left half and the structure of the secondary flow in the right half. From an overview of the figures it is seen that up to $PeRa \cong 10^5$ the main feature of the secondary flow field driven by natural convection is a general circulation that, in the case of heating, is upward directed adjacent to the inner cylinder wall. A stagnation point flow is developed at the bottom of the inner tube while at the top there is the formation of a plume ascending from the cylinder. At low $PeRa$ numbers, irrespective of the value of Pr , the secondary flow is expected to have a top-to-bottom symmetry about the horizontal centre-line. The $PeRa = 10^4$ streamline pattern is, indeed, virtually symmetric. The strength of the secondary flow increases as $PeRa$ increases, as witnessed by the numerical value of the dimensionless stream function f . Along with this, the eye of the eddy migrates toward the upper part of the annulus thus rendering the secondary flow field unsymmetrical and a circumferential boundary layer tends to develop near the heated wall. From the inspection of the structure of the flow, it is apparent how the fluid along the circumferential boundary layer first accelerates and then decelerates. At $PeRa \cong 10^5$ a small second eddy appears below the primary one, counter-rotating with respect to it. By increasing $PeRa$, size and strength of the secondary eddy increase, while remaining always less than those of the main eddy. From Eq. (8) it may be inferred that for $Pr \rightarrow \infty$ the advective terms vanish so that viscous diffusion and buoyancy forces dominate the secondary flow. The numerical results show that the effect of Pr on shape and strength of the secondary flow is weak and grows weaker as $PeRa$ decreases.

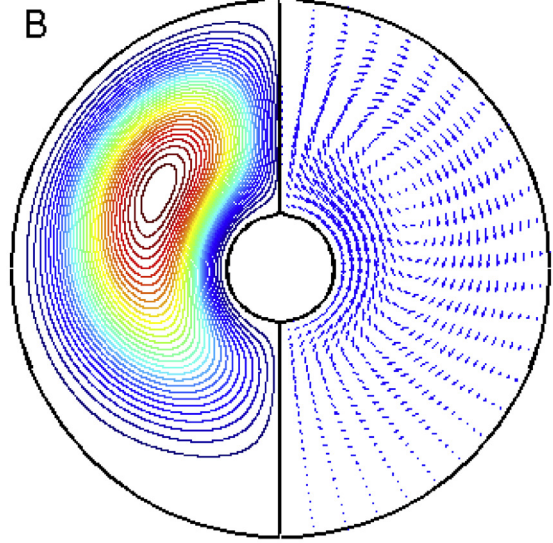
4.1.2. Axial velocity and mass flow rate

In the left part of Fig. 3 contour maps of the axial velocity are reported. From these figures it can be seen how the secondary flow induces a distortion of the axial velocity field with respect to the pure forced convection axial velocity profile. At a fixed Prandtl number, the distortion increases as $PeRa$ increases and the contours change their shape as a consequence of a more vigorous recirculation. At $PeRa = 10^4$ the axial velocity contours are almost concentric

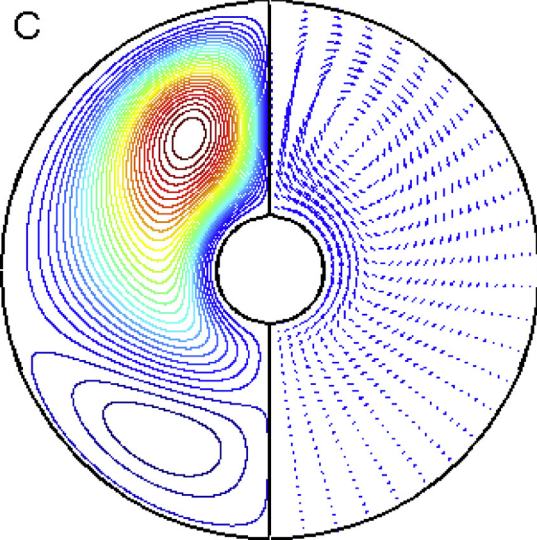
$$PeRa = 10^4; Pr = 0.7; f_{\max} = 0.75; f_{\min} = 0.00$$



$$PeRa = 10^5; Pr = 0.7; f_{\max} = 4.13; f_{\min} = -0.01$$



$$PeRa = 10^6; Pr = 0.7; f_{\max} = 11.74; f_{\min} = -1.30$$



$$PeRa = 10^7; Pr = 0.7; f_{\max} = 25.36; f_{\min} = -2.12$$

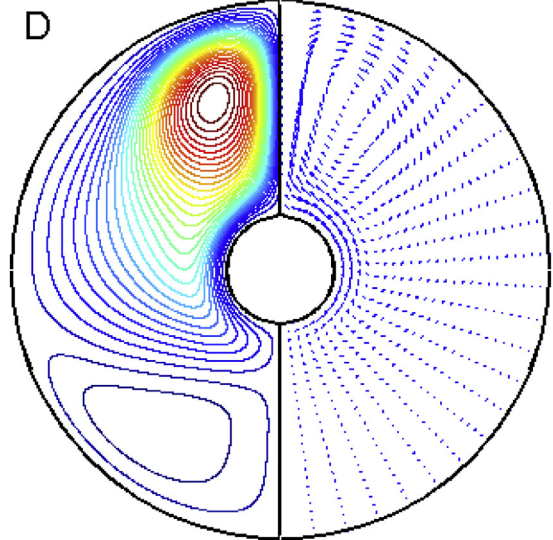


Fig. 2. Stream function contours (left) and velocity fields (right).

circles while at $PeRa = 10^7$ a considerable reorganization of the axial flow is evident. In Fig. 4 the influence of $PeRa$ at constant $Pr = 0.7$ on the axial velocity is presented. This figure shows the axial velocity, scaled with the average axial velocity, profile along the radial co-ordinate at three different angles, namely $\psi = 0$ (bottom), $\psi = \pi/2$ (centre) and $\psi = \pi$ (top) together with the axial velocity profile of pure forced convection. One can see that the distortion is such to increase the axial velocity at the bottom of the duct, while the opposite occurs at the top; consequently, the distribution of the axial shear stress is changed. On the contrary, increasing the Prandtl number at a fixed $PeRa$ hinders the distortion of the axial velocity field, as it is implied by Eq. (9). Fig. 5 compares the axial velocity field at $PeRa = 10^7$ and $Pr = 0.7$ and $Pr = 5$; this figure evidences the smoothing effect of increasing the Prandtl number.

A direct consequence of the modification of the axial shear stress due to the secondary flow is the reduction of the mass flow rate at a given axial pressure gradient. Letting the mass flow rate be denoted by \dot{m} , we have

$$\begin{aligned} \dot{m} &= 2 \int_{r_i}^{r_e} \int_0^\pi \rho w r \, dr \, d\psi = \rho \bar{w}^* r_e^2 \int_\eta^1 \int_0^\pi W R \, dR \, d\psi \\ &= 2\pi \rho \bar{w}^* r_e^2 \int_\eta^1 \left[W_0(R) + \sum_{j=1}^M C w_{0j} w_{0j} \Omega_{0j}(R) \right] R \, dR \\ &= \pi \rho \bar{w}^* r_e^2 (1 - \eta^2) \left[1 + \frac{2}{1 - \eta^2} \sum_{j=1}^M C w_{0j} w_{0j} \int_\eta^1 \Omega_{0j}(R) R \, dR \right] \\ &= \dot{m}_0 \left[1 + \frac{2}{1 - \eta^2} \sum_{j=1}^M C w_{0j} w_{0j} \int_\eta^1 \Omega_{0j}(R) R \, dR \right] \end{aligned} \quad (31)$$

where \dot{m}_0 is the mass flow rate for pure forced convection flow under the pressure gradient γ .

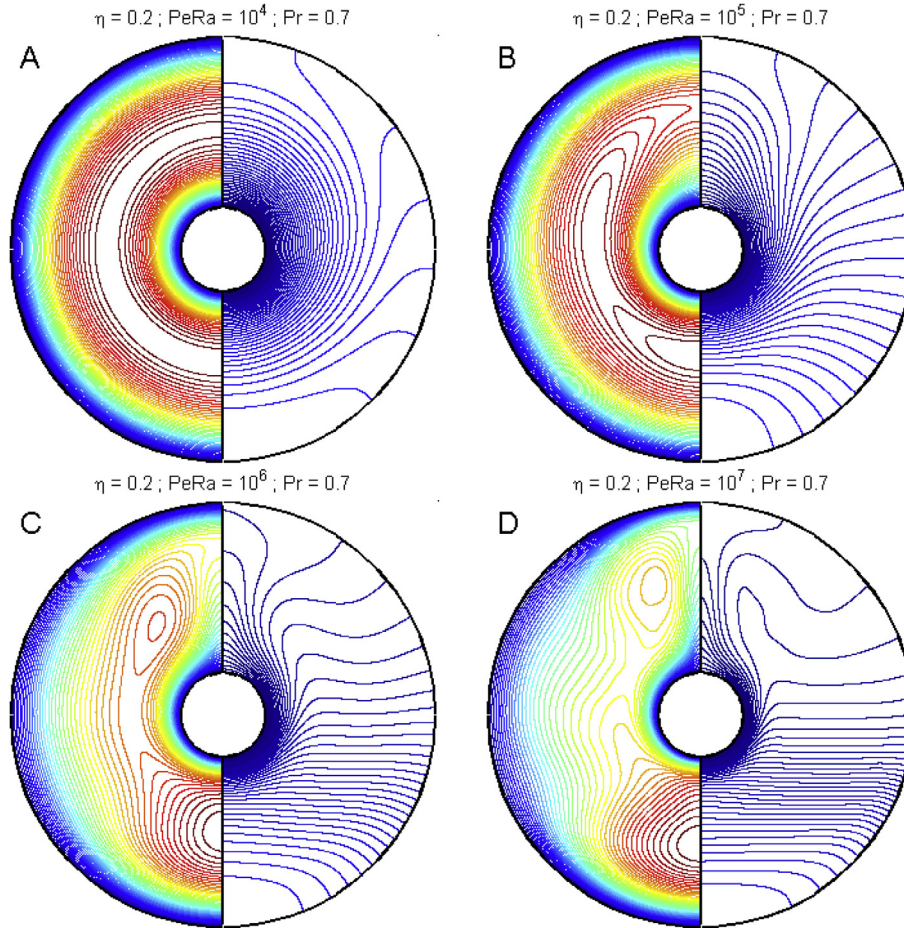


Fig. 3. Axial velocity (left) and temperature (right) contours.

The variation of the dimensionless mass flow rate \dot{m}/\dot{m}_0 with $PeRa$ parameterized by Pr is shown in Fig. 6. In accordance with what already discussed in connection with the behaviour of the axial velocity, we notice that the dimensionless mass flow rate is a decreasing function of $PeRa$ at a fixed Prandtl number, while, for a given $PeRa$, the increase in Pr causes a lesser reduction of \dot{m}/\dot{m}_0 . As a matter of fact, only for the case $Pr = 0.7$ does the dimensionless flow rate noticeably depart from unity. In the same figure, we have reported the results presented in graphical form by Nieckele and Patankar [5] for comparison purpose. These authors used slightly different dimensionless parameters with respect to the present work and presented the effect of the secondary flow on the axial velocity in terms of increase of the friction factor instead of reduction of the mass flow rate. However, it is easy to show that their Rayleigh number, Ra_{NP} , is related to the $PeRa$ number by the relationship $Ra_{NP} = \frac{1+\eta}{4\eta} \frac{\dot{m}}{\dot{m}_0} PeRa$ and that $\frac{fRe}{(fRe)_0} = \frac{\dot{m}_0}{\dot{m}}$, where here f is the friction factor and Re the Reynolds number computed on the basis of the actual mean axial velocity. The comparison shows an excellent agreement; in fact, the deviation never exceeds 1%.

4.1.3. Temperature field and heat transfer

Temperature field information, conveyed by isotherm maps, is displayed in the right part of Fig. 3 for representative cases. Up to $PeRa = 10^4$, irrespective to the value of Pr , near the heated surface the isotherms are practically concentric circles and thus heat transfer is faintly affected by the secondary motion. As $PeRa$

increases, the stronger recirculation changes the shape of the temperature contours and causes the accumulation of cold fluid in the lower part of the duct. From this ensues the crowding together of the isotherms near the lower part of the inner cylinder where a thermal boundary layer builds up at the higher $PeRa$ values. This reflects an increase of the local heat transfer rate in this region. On the contrary, near the top of the inner tube the isotherms become sparsely spaced and the local heat transfer rate goes through a minimum owing to the reverse stagnation point flow. A noteworthy feature of the temperature field, which is a direct consequence of the increasing strength of the secondary flow, is the tendency for the isotherms pattern to develop towards horizontal stratification, particularly in the region away from and under the inner cylinder, while near the heated bounding surface the thickness of the thermal boundary layer grows thinner. The effect of the Prandtl number on the temperature field is negligible for $PeRa$ values up to 10^5 . At higher values of $PeRa$ increasing the Prandtl number gives rise to a thinning of the thermal boundary layer, thus augmenting the heat transfer rate. Fig. 7 is intended to show the influence of the Prandtl number on the temperature field. It reports the distribution of the ratio between dimensionless local temperature and dimensionless bulk temperature along three radial lines with angles 0 , $\pi/2$, and π , at constant $PeRa = 10^7$. The evidence in this figure indicates indeed the decrease in thickness of the thermal boundary layer ($\psi = \pi/2$) and the increase in slope of the temperature distribution for $R = \eta$ taking place as the Prandtl number is raised.

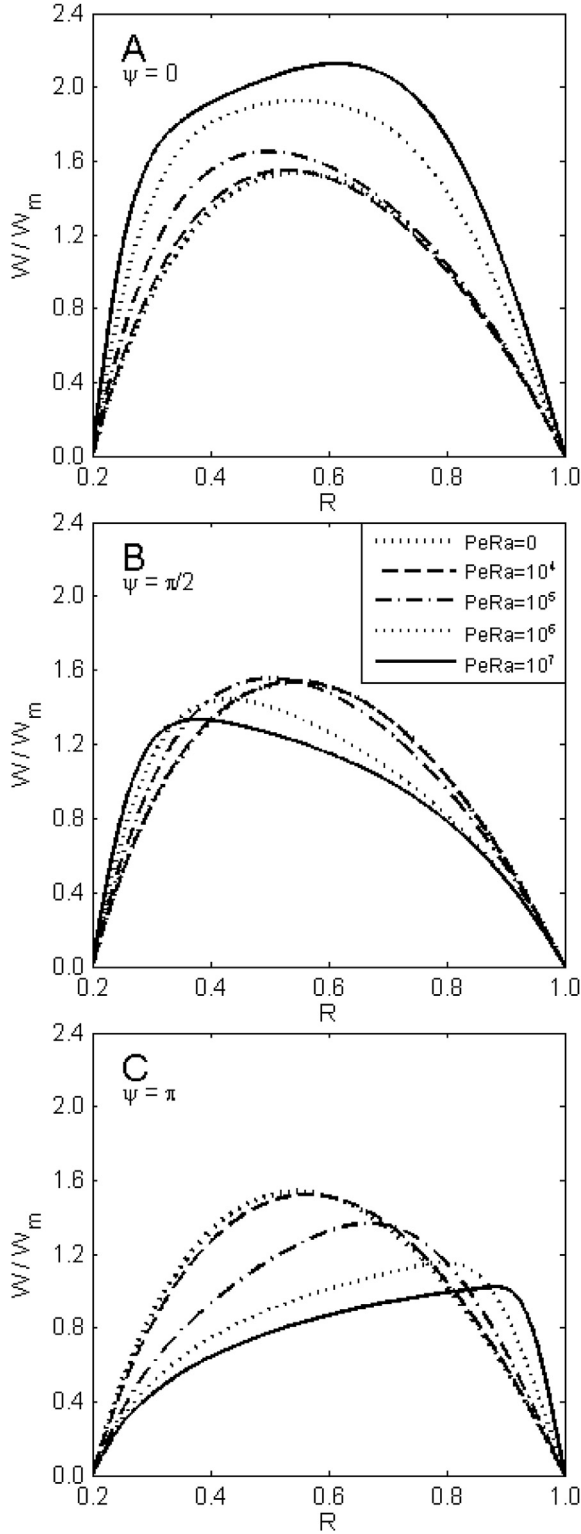


Fig. 4. Axial velocity, scaled with the average axial velocity, profiles along the radial coordinate for three values of the angular coordinate.

The effect of the secondary flow on heat transfer will now be examined. Let denote the local heat flux at the heated wall by q . From Fourier's law

$$q = -k \frac{\partial T}{\partial r} \Big|_{r=r_i} = \frac{k \Delta T^*}{r_e} \frac{\partial \vartheta}{\partial R} \Big|_{R=\eta} \quad (32)$$

and by definition of heat transfer coefficient h

$$q = h(T_w - T_m) = h \Delta T^* \vartheta_m \quad (33)$$

The following expression for the local Nusselt number is obtained

$$Nu = \frac{h D_H}{k} = 2(1 - \eta) \frac{\frac{\partial \vartheta}{\partial R} \Big|_{R=\eta}}{\vartheta_m} \quad (34)$$

T_m and ϑ_m denote bulk temperature and dimensionless bulk temperature, respectively, the latter being given by

$$\vartheta_m = \frac{\int_0^1 \int_0^\pi W \vartheta R \, dR \, d\psi}{\int_0^1 \int_0^\pi W R \, dR \, d\psi} \quad (35)$$

The angular variations of the ratio Nu/Nu_0 , where $Nu_0 = 8.499$ is the Nusselt number for the forced convection solution, are shown in Fig. 8 for selected values of $PeRa$ and Pr .

As expected on the basis of physical reasoning, a non-uniform local Nusselt number distribution is engendered as a result of natural convection which occurs together with forced convection and, owing to the structure of the secondary flow, a maximum appears at the bottom of the heated tube and a minimum at the top. It also appears that the higher the increase in heat transfer at the bottom, the higher the variation amplitude of the local Nusselt number along the periphery of the wall.

The average Nusselt number \overline{Nu} can be computed either according to its definition

$$\overline{Nu} = \frac{1}{\pi} \int_0^\pi Nu(\psi) \, d\psi \quad (36)$$

or from the integral energy balance, which gives

$$\dot{Q} = \dot{m} c \frac{\partial T}{\partial z} = \dot{m} c \tau = 2\pi r_i \bar{h} (T_w - T_m) \quad (37)$$

In the above equation \bar{h} and \dot{Q} denote average heat transfer coefficient and heat flow per unit length.

The forgoing, by substitution, leads to

$$\overline{Nu} = \frac{1 + \eta}{4\eta} \frac{\dot{m}}{\dot{m}_0} \frac{1}{\vartheta_m} \quad (38)$$

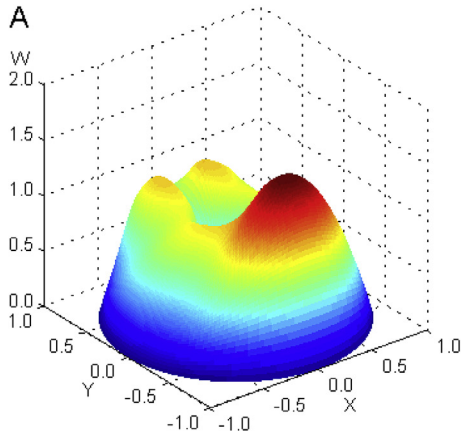
Both methods produce identical results to the fourth decimal digit, an issue that may be considered an indication of good accuracy of the solution.

Fig. 9 illustrates the change of the average Nusselt number \overline{Nu} divided by Nu_0 with $PeRa$ for different values of Pr .

In accordance with what suggested by the previous discussion, \overline{Nu} proves to be increasing both with $PeRa$ and Pr . However, the influence of $PeRa$ becomes noticeable only after a threshold value of approximately 10^4 is exceeded. Likewise, the influence of the Prandtl number manifests itself only for $PeRa$ values greater than 10^5 . The comparison with the results of Nieckele and Patankar [5] shows a good agreement; the discrepancy is at the very most equal to 3%. For this reason, calculations have been performed for only one value of the diameter ratio η .

The Nusselt number is shown in Fig. 10, as a function of $GrPr^{1.40}$ according to the Hattori correlation [1], which is also reported

Axial velocity distribution: effect of Prandtl number
 $PeRa = 10^7$; $Pr = 0.7$



Axial velocity distribution: effect of Prandtl number
 $PeRa = 10^7$; $Pr = 5.0$

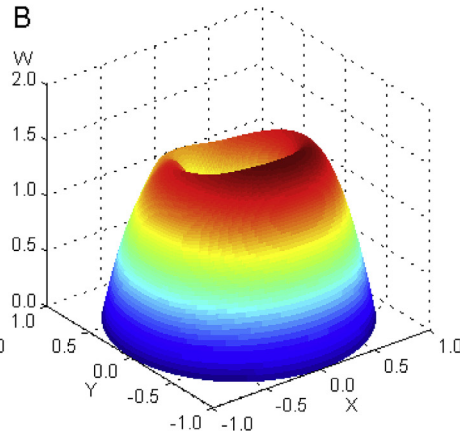


Fig. 5. Perspective plots of the axial velocity scaled with the average axial velocity.

together with a selection of experimental data. Moreover, the correlation by Ciampi et al. [7] has been reported for further comparison. The relation between $PeRa$ and $GrPr^{1.40}$ is given in Appendix. To compare the results it is worthwhile noting that most of Hattori's data refer to $\eta = 0.67$ (instead of 0.2) and water has been used as working medium, thus the Prandtl number is likely to be greater than unity. Then, it is expected that measured and calculated data show a different asymptotic value of the Nusselt number for pure forced convection. On the other hand, the difference lowers increasing $GrPr^{1.40}$ and the agreement becomes satisfactorily, although the numerical results show a lower rate of increase of the Nusselt number than the experimental data. As a consequence, in the range $10^9 < GrPr^{1.40} < 1.5 \times 10^{11}$ the deviation varies from -26% (overestimate) to $+18\%$ (underestimate). On the contrary, the results of Ciampi et al. [7] are quite different with respect to both the values of the Nusselt number and the rate of increase of Nu with $GrPr^{1.40}$. The former are considerably lower in all the Hattori's range (the lowest deviation is -41%) whereas the latter is much higher, so that acceptable agreement could be achieved extrapolating the Hattori correlation in the range $GrPr^{1.40} > 10^{15}$.

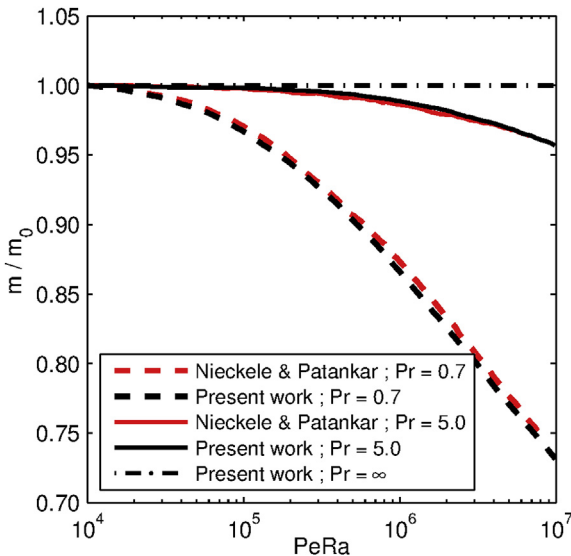


Fig. 6. Dimensionless mass flow rate as a function of $PeRa$ for various Pr .

4.2. Outer wall heated

The presentation of results will follow the same line used in the case of the inner wall heated.

4.2.1. Streamline maps and velocity field

Representative streamline maps and structure of the secondary flow are displayed in Fig. 11 for the three values of the ratio between the inner and the outer diameter, $PeRa$ equal to 10^4 and 10^7 , and $Pr = 0.7$ and ∞ . As in the case of heating from the inner duct, in

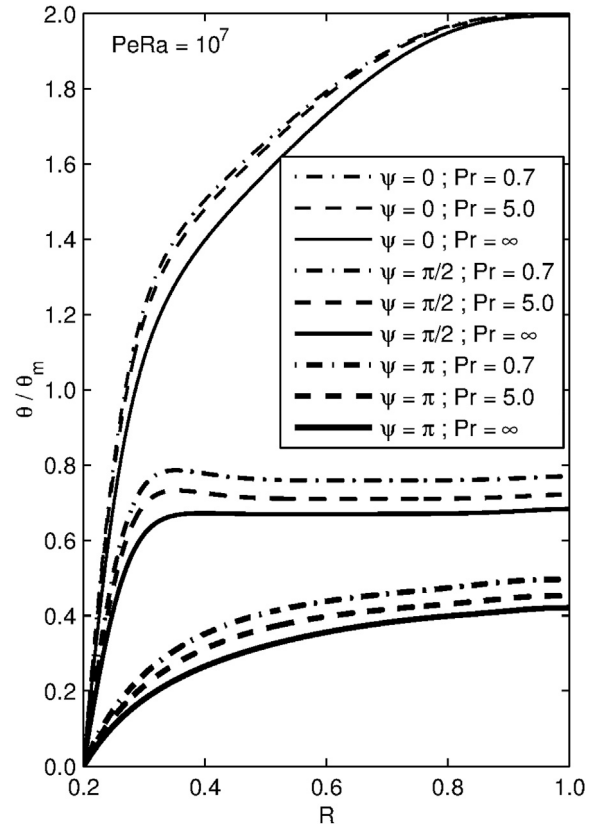


Fig. 7. Temperature, scaled with the bulk temperature, profiles along the radial coordinate for three values of the angular coordinate parameterized with Pr .

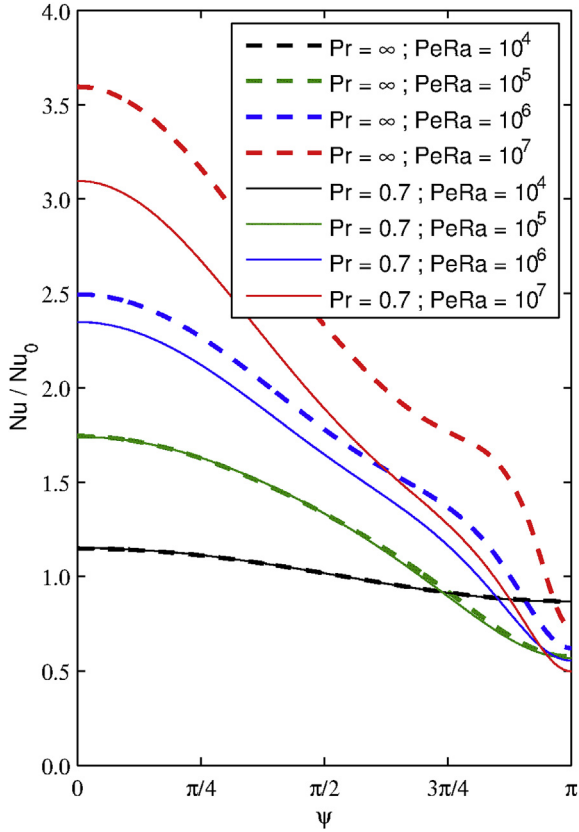


Fig. 8. Local Nusselt number, scaled with the pure forced convection Nusselt number, along the heated wall.

these figures the streamlines are plotted in the left half and the structure of the flow in the right half. From an overview of the figures it is seen that the main feature of the secondary flow driven by natural convection is a general circulation that, in the case of heating, is upward directed adjacent to the outer cylinder wall. Differently from the case of the inner wall heated, no second

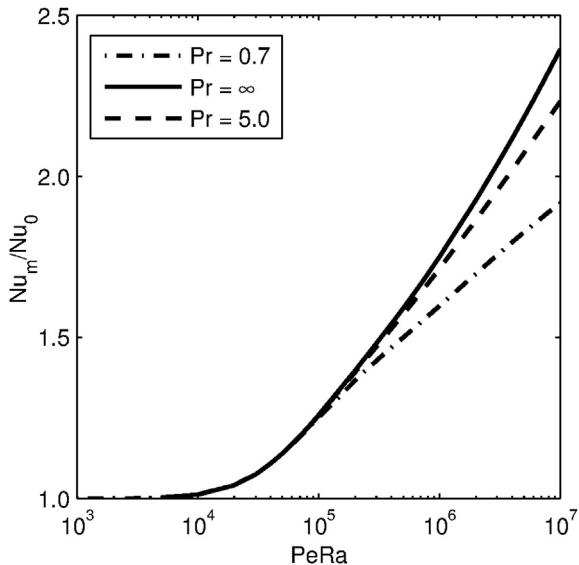


Fig. 9. Average Nusselt number, scaled with the pure forced convection Nusselt number, as a function of $PeRa$ parameterized with Pr .

eddies appear in the field, at least in the range of parameters explored in the present study. At low $PeRa$ numbers, irrespective of the value of Pr and η , the secondary flow is expected to have a top-to-bottom symmetry about the horizontal centre-line. The $PeRa = 10^4$ streamline patterns are, indeed, virtually symmetric for the three values of the ratio between inner and outer diameter and for all values of the Prandtl number. The strength of the secondary flow increases as $PeRa$ increases, at fixed values of η and Pr , as witnessed by the numerical value of the dimensionless stream function f . At fixed $PeRa$ and η , the strength of the recirculation increases as Pr increases, while, at fixed $PeRa$ and Pr , the recirculation strength grows weaker as η increases. As the strength of the recirculation increases, the structure of the secondary flow changes. The secondary flow becomes unsymmetrical because of the displacement of the eye of the eddy. At low values of the Prandtl number the migration is toward the upper part of the annulus while, at high values of Pr , the direction of the displacement re-verses and its extension diminishes as η increases. Along with this, a circumferential boundary layer tends to develop near the heated wall.

4.2.2. Axial velocity and mass flow rate

In the left part of Fig. 12 contour maps of the axial velocity for representative values of the parameters are reported. The effect of increased $PeRa$ at a finite value of Pr on the axial velocity is analogous to the one already discussed in the case of heating from the inner tube. One can see that the distortion of the axial velocity field due to the secondary flow is such to increase the axial velocity in the lower part of the annular channel and to lower it in the upper part, irrespective of the value of η . However, the maximum axial velocity does not occur in correspondence to the vertical mid-plane, but is displaced with respect to it. A three-dimensional perspective view of the complex structure of the axial velocity field is reported in Fig. 13. The effect of increased η at fixed $PeRa$ and Pr is to decrease the strength of the secondary flow and thus decrease the distortion of the axial velocity field with respect to the forced convection profile. Similarly, the Prandtl number increase at fixed $PeRa$ and η hinders the distortion of the axial velocity field. A direct consequence of the modification of the axial shear stress due to the secondary flow, is the reduction of the mass flow rate at a given axial pressure gradient. The variation of the dimensionless mass flow rate \dot{m}/\dot{m}_0 with $PeRa$ parameterized by Pr and η is shown in Fig. 14. In accordance with what already discussed in connection with the behaviour of the axial velocity, we notice that the dimensionless mass flow rate is a decreasing function of $PeRa$ at a fixed Prandtl number, while, for a given $PeRa$, the increase in Pr causes a lesser reduction of \dot{m}/\dot{m}_0 and so does the increase of η . As a matter of fact, only for the case $Pr = 0.7$ does the dimensionless flow rate noticeably depart from unity.

4.2.3. Temperature field and heat transfer

In the right part of Fig. 12 contour maps of the temperature field for representative values of the parameters are shown. Fig. 15 reports the three-dimensional perspective view of the temperature distribution, scaled with the bulk temperature, for $\eta = 0.4$, $PeRa = 10^7$, and $Pr = 0.7$. From these figures one can notice that for $PeRa = 10^4$ the isothermal lines are almost concentric circles, except close to the adiabatic inner tube where the secondary flow produces a distortion of the thermal field with respect to the pure forced convection temperature profile. By increasing $PeRa$ the reorganization of the temperature field due to the more vigorous recirculation becomes more and more evident. At the higher values of $PeRa$ the temperature field manifests the tendency to the formation of a thermal boundary layer close to the heated wall, the thickness of which diminishes as η is increased. Besides, one can

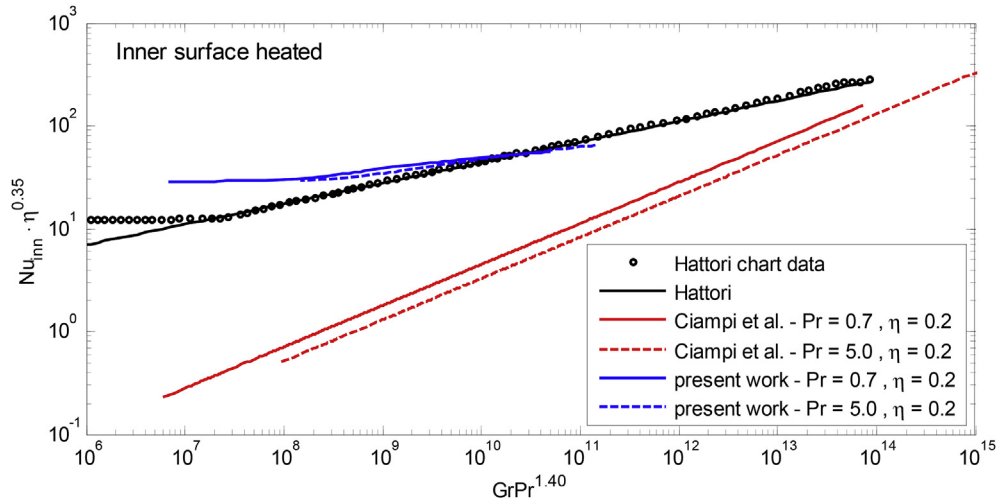


Fig. 10. Nusselt number as a function of $GrPr^{1.40}$, comparison between experimental data and correlation.

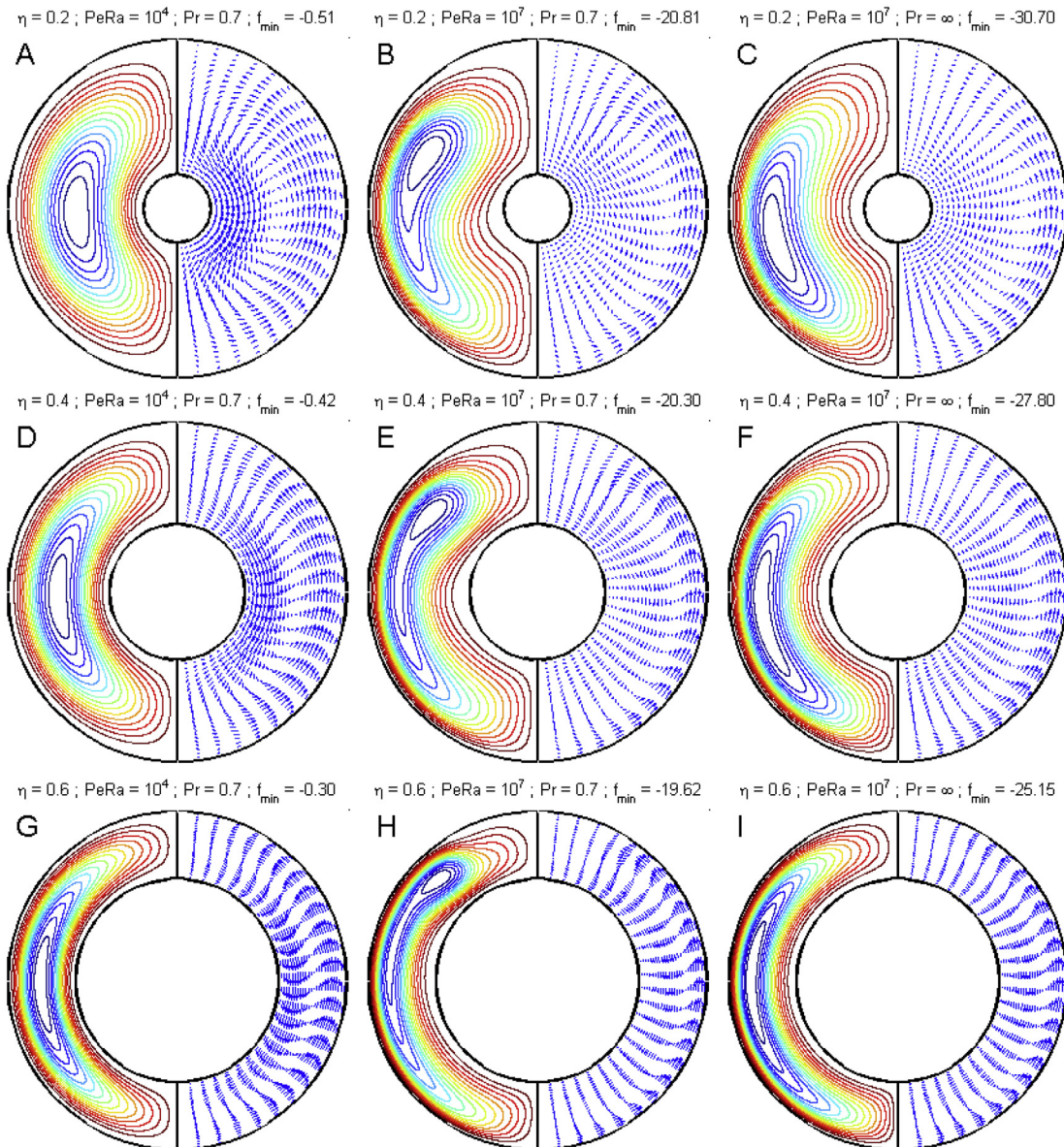


Fig. 11. Stream function contours (left) and velocity fields (right) for representative values of the parameters.

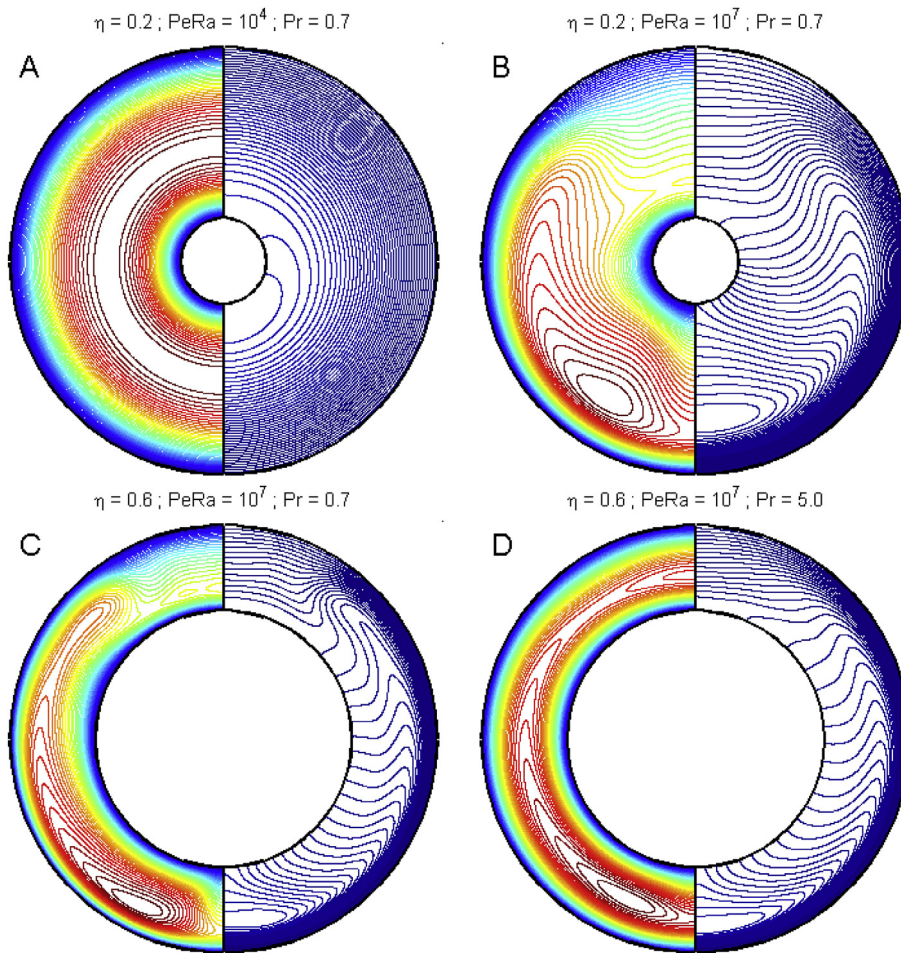


Fig. 12. Axial velocity (left) and temperature (right) contours for representative values of the parameters.

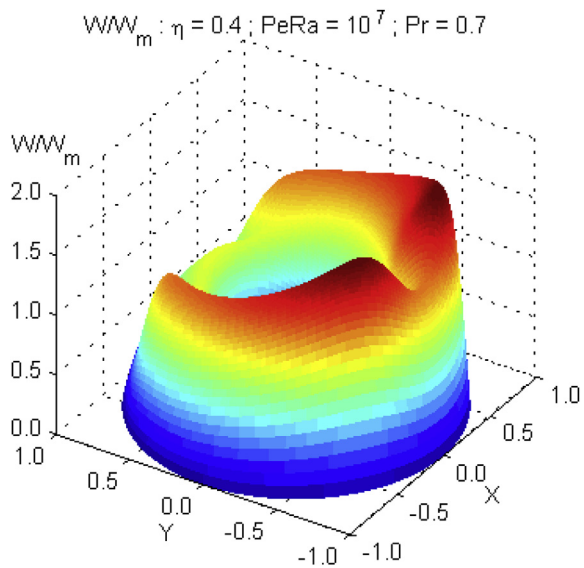


Fig. 13. Perspective plot of the axial velocity scaled with the average axial velocity.

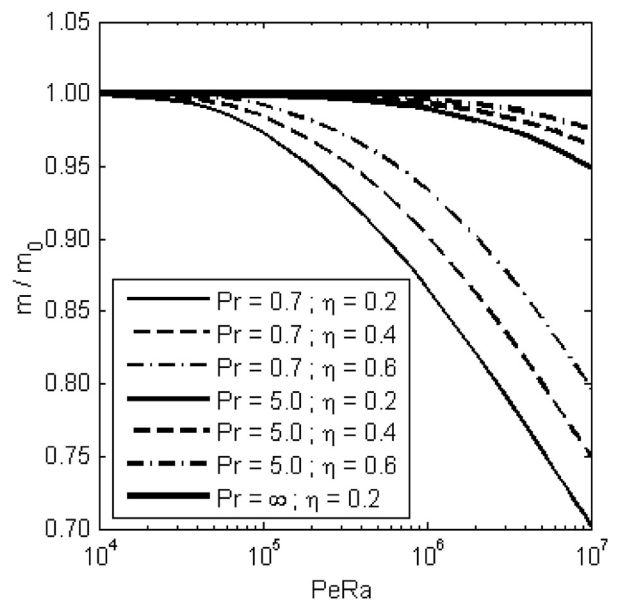


Fig. 14. Dimensionless mass flow rate as a function of $PeRa$ parameterized with Pr and η .

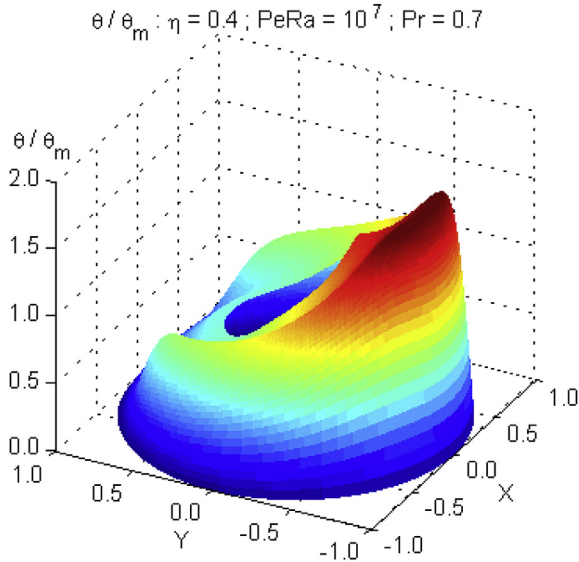


Fig. 15. Perspective plot of the temperature scaled with the bulk temperature.

notice the accumulation of cold fluid in the lower part of the annular duct and the tendency to the horizontal stratification of the temperature in the upper central part of the duct. The effect of increased Pr is to produce a flatter temperature profile in the core of the duct and to sharpen temperature gradients near the heated wall.

The local Nusselt number can be obtained by computing the radial temperature derivative at the heated wall and evaluating the bulk temperature according to a procedure similar to that one outlined for the inner wall heated. Examples of the local Nusselt number distribution along the heated wall are shown in Fig. 16. These figures report the ratio between the local Nusselt number,

Table 1

Fully developed Nusselt numbers for annular ducts.

η	Nu_0
0.2	4.883
0.4	4.979
0.6	5.099

Nu , and the Nusselt number in the pure forced convection, Nu_0 , as a function of the angular coordinate ψ . Nu_0 values are listed in Table 1.

As expected based on the preceding discussion, the maximum heat transfer takes place near the bottom of the channel; at the top of the channel, instead, the heat transfer goes through a minimum with values of Nu/Nu_0 even lower than unity. From the above mentioned figures, one can also appreciate the smoothing effect on the Nusselt number distribution of increasing Pr .

The average Nusselt number, Nu_m , can be obtained either by integrating the local Nusselt number distribution, or by means of the energy balance. According to the latter procedure, the following expression ensues

$$Nu_m = \frac{\dot{m}}{\dot{m}_0} \frac{1 + \eta}{4\vartheta_m} \quad (39)$$

As in the case of heating from the inner tube, both methods produce identical results to the fourth decimal digit. The effect of flow parameters on the average Nusselt number is shown in Fig. 17.

One can notice that the average Nusselt number is monotonically increasing with $PeRa$ and Pr . Furthermore the ratio Nu_m/Nu_0 decreases as η is increased.

The calculated values of the ratio Nu_m/Nu_0 can be interpolated by means of the following expression

$$\frac{Nu_m}{Nu_0} = 1 + \frac{0.121PeRa_{mod}^{2.320}}{1 + 1.164PeRa_{mod} + 0.432PeRa_{mod}^2} \quad (40)$$

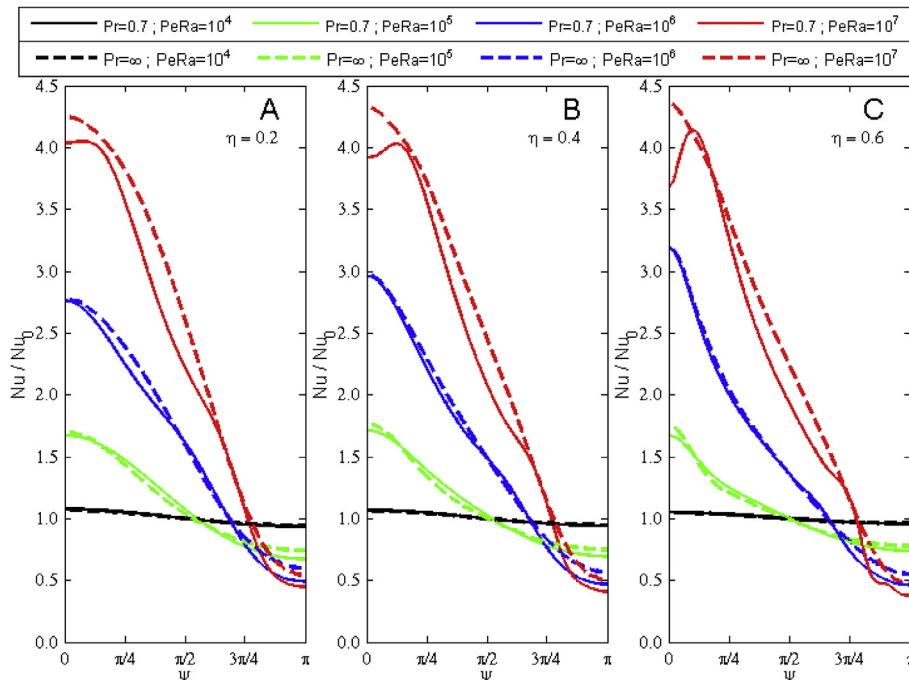


Fig. 16. Local Nusselt number, scaled with the pure forced convection Nusselt number, along the heated wall.

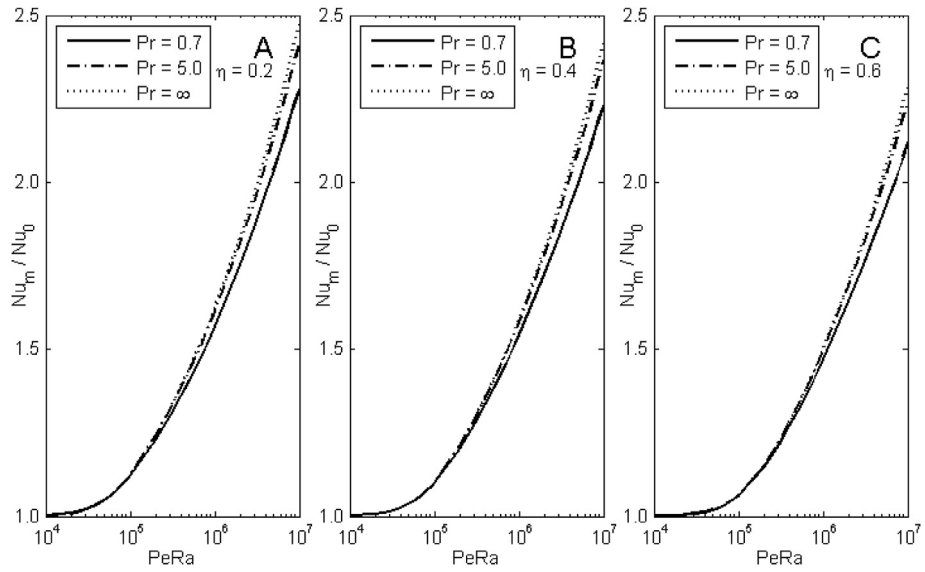


Fig. 17. Average Nusselt number, scaled with the pure forced convection Nusselt number, as a function of $PeRa$ parameterized with Pr and η .

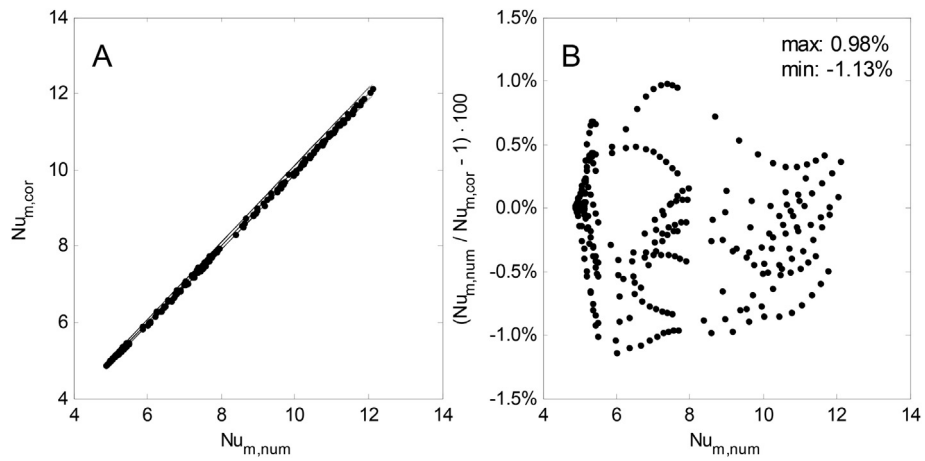


Fig. 18. Comparison between computed Nusselt number and prediction of the correlation.

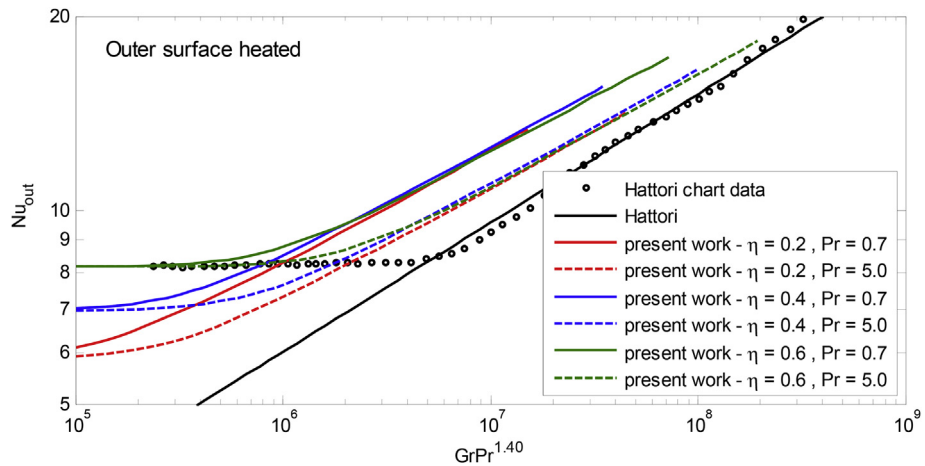


Fig. 19. Nusselt number as a function of $GrPr^{1.40}$, comparison between experimental data and numerical simulation reported in the present work.

where

$$PeRa_{\text{mod}} = (1 - \eta^2) PeRa^{m_1} m_2, \quad m_1 = 1 - \frac{0.074}{Pr^{0.437}},$$

$$m_2 = \frac{1}{5 \cdot 10^4} \left(1 + \frac{1.342}{Pr^{0.542}} \right)$$

within the ranges $0.2 \leq \eta \leq 0.6$, $0.7 \leq Pr < \infty$, $PeRa \leq 107$.

As it can be seen in Fig. 18, the proposed correlation predicts the data with deviations, between the numerical results ($Nu_{m,num}$) and predicted values ($Nu_{m,corr}$), in the range $[-1.13\%, 0.98\%]$.

The Nusselt number is shown in Fig. 19, as a function of $GrPr^{1.40}$ according to the Hattori's correlation, which is also reported together with a selection of experimental data. The relation between $PeRa$ and $GrPr^{1.40}$ is given in Appendix. To compare the results it is worthwhile noting that most of Hattori's data refer to $\eta = 0.67$ and water has been used as working medium, thus the Prandtl number is expected to be greater than unity. The numerical results corresponding to the most similar conditions, i.e. $\eta = 0.6$ and $Pr = 5$, agree with the experimental data within 10%, both in the asymptotic region corresponding to the limit of pure forced convection and in the mixed convection region. The same is observed for the Hattori's correlation that only holds in the mixed convection region.

5. Conclusions

Fully developed laminar mixed convection in horizontal annular ducts has been studied numerically through a spectral method. Two sets of boundary conditions have been investigated, namely uniform temperature at the inner cylinder, thermal insulation at the outer one (a), and vice versa (b). As suggested by the dimensional analysis of the problem, the inner to outer radius ratio, η , the product between Péclet and Rayleigh numbers, $PeRa$, and Prandtl number, Pr , have been assumed as relevant parameters in the description of the flow and temperature fields, which are significantly affected by the different boundary conditions. Though in both cases the secondary flow field driven by free convection is a general circulation symmetric about the vertical mid plane, in case (a) for $PeRa \geq 10^5$ a second eddy appears below the main one (inner cylinder heated), counter-rotating with respect to it and growing in dimensions and strength by increasing $PeRa$. On the contrary, in case (b) any secondary vortex is not observed within the explored range of the parameters. Anyway, the main effect of the secondary flow is a distortion of the axial velocity profile compared to the case of pure forced convection, which causes a reduction of the mass flow rate at a given axial pressure gradient. This effect is less pronounced for high values of η (i.e. for narrow annuli) and is appreciable only at low Pr and for $PeRa \geq 10^5$. Concerning the temperature field, in both cases a thermal boundary layer tends to develop past the heated surface, becoming thinner as $PeRa$ increases. However, in case (a) a plume rises from the inner cylinder and, by increasing $PeRa$, a horizontal stratification of temperature is observed in the lower region. On the contrary, in case (b), the circulation promotes a horizontal stratification of temperature in the upper region. Consequently, the heat transfer rate is unevenly distributed around the girth of the heated tube, showing in both cases a maximum near the bottom and a minimum at the top. The Nusselt number is greater than it is for pure forced convection (up to a factor 2.5 in the investigated range of the parameters). Furthermore, at constant $PeRa$ and η , the Nusselt number increases with Pr , but the influence of Pr is more evident for $PeRa \geq 10^5$.

Nomenclature

Latin symbol

c	specific heat [J kg ⁻¹ K ⁻¹]
Cf_{ij}	normalization coefficient [-]
Ct_{ij}	normalization coefficient [-]
CW_{ij}	normalization coefficient [-]
D_H	hydraulic diameter [m]
f	non dimensional stream function [-]
f°	initial guess of the non dimensional stream function [-]
f_{ij}	unknown coefficient of the trial functions [-]
g	gravitational acceleration [m s ⁻²]
Gr	Grashof number [-]
h	local heat transfer coefficient [W m ⁻² K ⁻¹]
\bar{h}	average heat transfer coefficient [W m ⁻² K ⁻¹]
i	counter [-]
j	counter [-]
k	thermal conductivity [W m ⁻¹ K ⁻¹]
L_T	characteristic length [m]
M	last term of the truncated expansion [-]
\dot{m}	mass flow rate [kg s ⁻¹]
\dot{m}_0	mass flow rate for pure forced convection [kg s ⁻¹]
m_1	function of Pr introduced to simplify the equation expression [-]
m_2	function of Pr introduced to simplify the equation expression [-]
N	last term of the truncated expansion [-]
Nu	Nusselt number [-]
\bar{Nu}	average Nusselt number [-]
Nu_0	Nusselt number for the forced convection [-]
Nu_{inn}	average Nusselt number for the inner wall heated case [-]
Nu_{out}	average Nusselt number for the outer wall heated case [-]
Nu_{D_h}	Nusselt number referred to the hydraulic diameter [-]
Nu_{L_T}	Nusselt number referred to the characteristic length [-]
Nu_m	average Nusselt number [-]
P	non dimensional pressure [-]
p	pressure [Pa]
p^*	pressure scale [Pa]
Pe	Péclet number [-]
P_{j+1}	Legendre polynomials [-]
$PeRa_{\text{mod}}$	function of Pe , Ra , m_1 , m_2 and η introduced to simplify the equation expression [-]
Pr	Prandtl number [-]
\dot{Q}	heat flow per unit length [W m ⁻¹]
q	heat flux [W m ⁻²]
\bar{q}	average heat flux [W m ⁻²]
q_e	heat flux imposed on the outer tube [W m ⁻²]
q_i	heat flux imposed on the inner tube [W m ⁻²]
R	non dimensional radial coordinate [-]
r	radial coordinate [m]
Ra	Rayleigh number [-]
Ra^*	modified Rayleigh number [-]
Ra_{NP}	Rayleigh number according to Niecele and Patankar [-]
Re	Reynolds number [-]
r_e	inner radius of the outer pipe [m]
r_i	outer radius of the inner pipe [m]
T	temperature [K]
T_m	bulk temperature [K]
t_{ij}	unknown coefficients of the truncated expansions [-]
T_w	local temperature of the inner pipe wall [K]
U	non dimensional velocity component along the radial direction [-]
u	velocity component along the radial direction [m s ⁻¹]

V	non dimensional velocity component along the angular coordinate [–]
v	velocity component along the angular coordinate [m s ⁻¹]
W	non dimensional velocity component along the axial coordinate [–]
w	velocity component along the axial coordinate [m s ⁻¹]
\bar{w}	actual mean axial velocity [m s ⁻¹]
\bar{w}^*	average velocity for laminar flow through an unheated annular duct [m s ⁻¹]
W ₀	non dimensional axial velocity distributions in the absence of natural convection [–]
W _m	non dimensional mean axial velocity [–]
w _{ij}	unknown coefficients of the truncated expansions [–]
z	axial coordinate [m]

Greek symbols

α	thermal diffusivity [m ² s ⁻¹]
β	coefficient of thermal expansion [K ⁻¹]
γ	pressure gradient along the axial coordinate [Pa m ⁻¹]
δ	function of η introduced to simplify the equation expression [–]
ΔT^*	temperature scale [K]
ε	function of η introduced to simplify the equation expression [–]
ζ	convergence parameter [–]
η	ratio of the outer radius of the inner pipe over inner radius of the outer pipe [–]
θ	non dimensional temperature [–]
θ°	initial guess of the non dimensional temperature [–]
θ_0	non dimensional temperature distributions in the absence of natural convection [–]
Θ_{ij}	trial functions for temperature [–]
θ_{ij}	unknown coefficients of the truncated expansions [–]
θ_m	non dimensional bulk temperature [–]
μ	dynamic viscosity [kg s ⁻¹ m ⁻¹]
ν	kinematic viscosity [m ² s ⁻¹]
ξ	function of R and η introduced to simplify the equation expression [–]
ρ	density in the reference state [kg m ⁻³]
τ	temperature gradient along the axial coordinate [K m ⁻¹]
Φ_j	radial trial functions for stream functions [–]
Ψ_{ij}	trial functions for stream functions [–]
ψ	angular coordinate [rad]
Ω_{ij}	trial functions for axial velocity [–]
ω	relaxation parameter [–]

Mathematical symbols

Δ^2	biharmonic operators
Δ	Laplace operators
J	Jacobian operator
(\cdot, \cdot)	inner product

Appendix

According to Hattori [1] the characteristic length appearing in the dimensionless groups is defined as

$$L_T = \frac{2(r_e^2 - r_i^2)(q_e + q_i)}{r_e q_e + r_i q_i} = \frac{D_H(1 + \eta)(q_e + q_i)}{q_e + \eta q_i}$$

where q_e and q_i are heat fluxes imposed on outer and inner tubes, respectively.

Consequently, the relationship between the Nusselt number referred to the hydraulic diameter, Nu_{D_H} and that one referred to L_T , Nu_{L_T} , is

$$\frac{Nu_{D_H}}{Nu_{L_T}} = \frac{D_H}{L_T}$$

The Grashof number appearing in Hattori's paper is defined as

$$Gr = \frac{\beta g \bar{w} \tau L_T^5}{\alpha \nu^2}$$

where \bar{w} is the actual mean axial velocity.

The relationship between $PeRa$ and Gr reads as follows

$$\frac{PeRa}{Gr} = \frac{\dot{m}_0}{\dot{m}} \left(\frac{D_H}{L_T} \right)^5 Pr$$

Ciampi et al. [7] assume D_H as the characteristic length appearing in the dimensionless groups they define.

The modified Rayleigh number, Ra^* , is

$$Ra^* = Pr \frac{\beta g \bar{q} D_H^4}{k \nu^2}$$

where \bar{q} is the average heat flux.

From the energy balance one has

$$\bar{q} = \frac{D_H}{4} \left(\frac{1 + \eta}{\eta} \right) \rho C \tau \bar{w}$$

Therefore, the relationship between Ra^* and Gr reads as follows

$$\frac{Ra^*}{Gr} = \frac{Pr}{4} \frac{1 + \eta}{\eta} \left(\frac{D_H}{L_T} \right)^5$$

References

- [1] N. Hattori, Combined free and forced convection heat transfer for fully developed laminar flow in concentric annuli, numerical analysis, Trans. JSME 45 (1979) 227–239.
- [2] A. Mojtabi, J.P. Caltagirone, Analyse du transfer de chaleur en convection mixte laminaire entre deux cylindres coaxiaux horizontaux, Int. J. Heat Mass Transf. 23 (1980) 1369–1375.
- [3] T.H. Nguyen, P. Vasseur, L. Robillard, B. Shekhar, Combined free and forced convection heat transfer of water between horizontal concentric annuli, J. Heat Transf. 105 (1983) 498–500.
- [4] S. Kotake, N. Hattori, Combined free and forced convection heat transfer for fully developed laminar flow in concentric annuli, Int. J. Heat Mass Transf. 28 (11) (1985) 2115–2120.
- [5] A. Niecele, S.W. Patankar, Mixed convection in a concentric annulus with horizontal axis, J. Heat Transf. 107 (1985) 902–909.
- [6] M. Kaviani, Laminar combined convection in a horizontal annulus subject to constant heat flux inner wall and adiabatic outer wall, Trans. ASME J. Heat Transf. 108 (1986) 392–397.
- [7] M. Ciampi, S. Faggiani, W. Grassi, F.P. Incropera, G. Tuoni, Experimental study of mixed convection in horizontal annuli for low Reynolds number, in: Proc. 8th Int. Heat Transfer Conference, vol. 3, 1986, pp. 1413–1418.
- [8] K.C. Karki, S.V. Patankar, Laminar mixed convection in the entrance region of a horizontal annulus, Numer. Heat Transf. 15 (1989) 87–99.
- [9] C. Nonino, S. Del Giudice, Finite element analysis of laminar mixed convection in the entrance region of horizontal annular ducts, Numer. Heat Transf. Part A 29 (1996) 313–330.
- [10] Nazrul Islam, U.N. Gaitonde, G.K. Sharma, Combined free and forced convection in a horizontal annulus, in: Proc. 11th Int. Heat Transfer Conference, vol. 3, 1998, pp. 299–304.
- [11] H.A. Mohammad, A. Campo, R. Saidur, Experimental study of forced and free convective heat transfer in the thermal entry region of horizontal concentric annuli, Int. Comm. Heat Mass Transf. 37 (2010) 739–747.
- [12] Nazrul Islam, U.N. Gaitonde, G.K. Sharma, Mixed convection heat transfer in the entry region of horizontal annuli, Int. J. Heat Mass Transf. 44 (2001) 2107–2120.
- [13] Joo-Sik Yoo, Mixed convection of air between two horizontal concentric cylinders with a cooled rotating outer cylinder, J. Heat Mass Transf. 41 (1998) 293–302.

- [14] C. Nouar, Numerical solution for laminar mixed convection in a horizontal annular duct: temperature-dependent viscosity effect, *Int. J. Numer. Meth. Fluids* 29 (1999) 849–864.
- [15] C. Nouar, B. Bernaouda-Zouaoui, C. Desaubry, Laminar mixed convection in a horizontal annular duct. Case of thermodependent non-Newtonian fluid, *Eur. J. Mech. B Fluids* 19 (2000) 423–452.
- [16] M.A. Habib, A.A.A. Negm, Laminar mixed convection in horizontal concentric annuli with non-uniform circumferential heating, *Heat Mass Transf.* 32 (2001) 427–435.
- [17] E. Chenier, G. Petrone, G. Lauriat, From natural to mixed convection in horizontal and differentially heated annular ducts: linear stability analysis, *J. Heat Mass Transf.* 54 (23–24) (2011) 5100–5108.
- [18] R.K. Shah, A.L. London, *Laminar Flow Forced Convection in Ducts*, Academic Press, San Francisco, California, 1978.
- [19] B.R. Morton, Laminar convection in uniformly heated horizontal pipes at low Rayleigh numbers, *Quart. J. Mech. Appl. Math.* 12 (1959) 410–420.
- [20] R.B. Bird, W.E. Stewart, E.N. Lightfoot, *Transport Phenomena*, second ed., John Wiley & Sons, New York, 2002.
- [21] C. Canuto, M.Y. Hussdini, A. Quarteroni, T.A. Zang, *Spectral Methods in Fluid Dynamics*, Springer–Verlag, 1988.
- [22] S.G. Mikhailin, *The Numerical Performance of Variational Methods*, Wolters–Noordhoff Publishing, 1971.